Langmuir

Article

pubs.acs.org/Langmuir

Cancer-Cell-Targeted Theranostic Cubosomes

Claudia Caltagirone,*[,†] Angela Maria Falchi,[‡] Sandrina Lampis,[†] Vito Lippolis,[†] Valeria Meli,[†] Maura Monduzzi,[†] Luca Prodi,[§] Judith Schmidt,[∥] Massimo Sgarzi,[§] Yeshayahu Talmon,[∥] Ranieri Bizzarri,[⊥] and Sergio Murgia*[,†]

[†]Dipartimento di Scienze Chimiche e Geologiche and [‡]Dipartimento di Scienze Biomediche, Università di Cagliari, s.s. 554 bivio Sestu, I-09042 Monserrato, CA, Italy

[§]Dipartimento di Chimica "G. Ciamician" Università degli Studi di Bologna, via Selmi 2, 40126 Bologna, Italy

[∥]Department of Chemical Engineering, Technion − Israel Institute of Technology, Haifa 32000, Israel

[⊥]Istituto di Biofisica, CNR, U.O. Pisa, Via G Moruzzi 1, 56124 Pisa, Italy

Supporting Information

ABSTRACT: This work was devoted to the development of a new type of lipid-based (cubosome) theranostic nanoparticle able to simultaneously host camptothecin, a potent anticancer drug, and a squarain-based NIR-emitting fluorescent probe. Furthermore, to confer targeting abilities on these nanoparticles, they were dispersed using mixtures of Pluronic F108 and folate-conjugated Pluronic F108 in appropriate ratios. The physicochemical characterization, performed via SAXS, DLS, and cryo-TEM techniques, proved that aqueous dispersions of such cubosomes can be effectively prepared, while the photophysical characterization demonstrated that these nanoparticles may be used for in vivo imaging purposes. The superior ability of these innovative nanoparticles in targeting cancer cells was emphasized by investigating the lipid droplet alterations induced in HeLa cells upon exposure to targeted and nontargeted cubosomes.

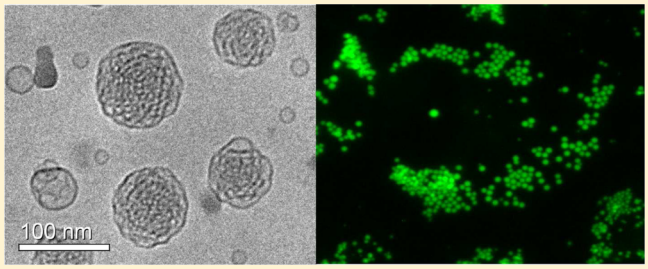

INTRODUCTION

The main goal of nanomedicine is probably the improvement of diagnostic and therapeutic tools available in clinics. Therefore, considerable efforts has been made to develop the physicochemical and biological characteristics of the nanocarriers engineered to encapsulate drugs or imaging agents with pharmaceutical purposes. Since nanocarriers may be formulated using an extensive range of organic and inorganic materials, these efforts resulted in the assembly of a huge number of "soft" and "hard" nanocarriers, such as polymeric,[1−5] silica,[6,7] or iron oxide nanoparticles,[8−10] liposomes,[11−13] dendrimers,[10,14,15] and quantum dots.[16−18] Recently, the development of single platforms able to simultaneously transport and release pharmaceutically active and imaging agents has led to so-called theranostic nanoparticles. Besides, the latter usually contain a targeting ligand as a third component to specifically direct both the therapeutic and diagnostic agents to the pathological site. In principle, these multifunctional nanocarriers should fulfill a number of requisites that include the controlled (co)delivery of poorly water-soluble (multiple) drugs, the selective targeting of malignant cells for minimizing side effects, and the in-progress evaluation of the treatment efficacy via molecular detection.[19−29]

The accumulation of nanoparticles in tumor tissues passively occurs as a result of aberrant tumor angiogenesis that forms nonmature, leaky capillaries. Indeed, the primary consequences of the defects in tumor vessels are great permeability to colloidal macromolecules or nanoparticles in comparison to physiological vessels and reduced lymphatic drainage of these colloids from the interstitial space of tumors, a phenomenon called the enhanced permeation and retention (EPR) effect.[30] Conversely, nanoparticles may be actively targeted to tumor tissues employing cancer-cell-specific ligands such as folic acid. The popularity of this ligand has mainly grown because cancer cells frequently overexpress folate receptors (which is the case for ovary, breast, brain, kidney, head, neck and other tumors) and because of its high binding affinity, ease of modification, stability during storage, and low cost.[31,32]

Fluorescent imaging is one of the most powerful techniques in clinical diagnosis[33] for monitoring biological processes in living systems due to its characteristics of high spatial and temporal resolution. Contrast agents such as Gd^{3+} complexes[34] and fluorodeoxyglucose[35] are widely used in MRI (magnetic resonance imaging) and PET (positron emission tomography). In the last few decades, a profusion of fluorescent probes has been developed by synthesis chemists. However, most of them can hardly be used for in vivo applications because the majority of the conventional fluorophores emit in the UV−vis region.

Received: April 7, 2014
Revised: May 9, 2014
Published: May 12, 2014

   dx.doi.org/10.1021/la501332u | *Langmuir* 2014, 30, 6228−6236

Indeed, in this portion of the electromagnetic spectrum the absorption of biomolecules (water, hemoglobin, etc.), the autofluorescence of the cells, and the light scattering are high, causing limited tissue penetration as well as low signal-to-noise ratios, resulting in unsuitability for in vivo imaging. Conversely, dyes active in the NIR (near infrared) region of the spectrum (650−900 nm) have attracted much attention because of minimum photodamage to biological samples, deep tissue penetration, and minimum interference from background autofluorescence by biomolecules in living systems.[36−38] Different classes of NIR-emitting fluorophores have been developed such as phtalocyanines, cyanines, and squaraines. In particular, the latter[39] are the dicondensation products of electron-rich molecules with squaric acid and are characterized by a sharp and intense low-energy absorption associated with strong fluorescence in solution.

Among the various nanocarriers engineered for theranostic nanomedicine, cubosomes have been only recently proposed.[40] Basically, these are aqueous dispersions of lipid-based bicontinuous liquid-crystalline phases typically stabilized by Pluronics.[41,42] Therefore, the inner nanostructure of the nanoparticles is constituted of curved, triply periodic non-intersecting bilayers folded on an infinite periodic minimal surface of cubic symmetry and organized to form two disjointed continuous water channels.[43,44]

Throughout this article it will be shown that cubosome nanoparticles coloaded with both an NIR fluorescent probe and an anticancer drug can be prepared and effectively stabilized by mixtures of F108 and folate-conjugated F108 Pluronics that give these nanoparticles superior targeting ability toward HeLa cancer cells with respect to traditional cubosomes.

EXPERIMENTAL SECTION

Chemicals. Monoolein (MO, 1-monooleoylglycerol, RYLO MG 19 PHARMA, glycerol monooleate, 98.1 wt %) was kindly provided by Danisco A/S, DK-7200, Grinsted, Denmark. Pluronic F108 (PEO_{132}−PPO_{50}−PEO_{132}), folic acid (≥97%), camptothecin (≥90%), 2,4-di-3-guaiazulenyl-1,3-dihydroxycyclobutenediylium dihydroxide bis(inner salt), acetonitrile (≥99.9%), diethyl ether (≥99.5%), *N*,*N*′-carbonyldiimidazole (CDI, ≥ 97%), ethylenediamine, (≥99.5%), *N*-hydroxysuccinimmide (NHS, 98%), *N*,*N*′-dicyclohexylcarbodiimide (DCC, ≥ 99.5%), and triethylamine (≥99.5%) were purchased from Sigma-Aldrich. Distilled water passed through a Milli-Q water-purification system (Millipore) was used to prepare the samples.

Nuclear Magnetic Resonance Experiments. ^{1}H NMR measurements were performed on a Bruker Avance 300 MHz (7.05 T) spectrometer at an operating frequency of 300.131 MHz at 25 °C. A standard variable-temperature control unit with an accuracy of ±0.5 °C was used. Chemical shifts for ^{1}H NMR are reported in parts per million (ppm), with coupling constants reported in Hertz (Hz). The following abbreviations are used for spin multiplicity: s, singlet; d, doublet; t, tripletl and m, multiplet. A selection of the characteristic ^{1}H signals are reported in the synthesis of F108-CDI, F108-NH_2, and F108-FA Pluronics.

Synthesis of Folate-Conjugated Pluronic F108. *Synthesis of CDI-Activated Pluronic F108 (F108-CDI).* To a solution of Pluronic F108 (2.01 g, 0.14 mmol) in dry acetonitrile (10 mL), a solution of a great excess of *N*,*N*′-carbonyldiimidazole (CDI, 0.26 g, 1.6 mmol) in dry acetonitrile (5 mL) was added dropwise during a period of 45 min. The mixture was kept stirring at room temperature under a nitrogen atmosphere for 6 h. Then, the solution was concentrated in a rotary evaporator and washed with diethyl ether (3 × 10 mL) to remove unreacted CDI. The product was dried under vacuum and collected as a white powder. Yield: 93% (1.890 g, 0.13 mmol); mp: 54 °C. ^{1}H NMR (300 MHz, DMSO-d_6, 298 K): δH 1.03 (d, J = 6 Hz; 3H × 50, $-CH_3$ of PPO), 3.47−3.54 (m, 3H × 50, 4H × 264, $-CH_2-CH(CH_3)-O-$ of PPO and $-CH_2-CH_2-O-$ of PEO), 7.50−7.65 (m, 2H × 2, protons of the imidazole moiety), 8.25 (s, 1H × 2, proton of the imidazole moiety). IR (solid state, cm^{-1}) ν = 2885 (s), 1743 (w).

Synthesis of NH_2-Terminated Pluronic F108 (F108-NH_2). To a solution of F108-CDI (1.010 g, 0.068 mmol) in dry acetonitrile (10 mL), 0.78 mL of ethylenediamine was added. The reaction mixture was kept stirring for 24 h at room temperature under a nitrogen atmosphere. The solvent and unreacted ethylenediamine were removed under vacuum. The crude product was precipitated with diethyl ether and collected as a beige powder. Yield: 81% (0.813 g; 0.055 mmol); mp: 56 °C. ^{1}H NMR (300 MHz, DMSO-d_6, 298 K): δH 1.03 (d, J = 6 Hz, 3H × 50, $-CH_3$ of PPO), 2.65−2.75 (m, 2H × 2 protons adjacent to the terminal amine), 2.96 (q, J = 6 Hz, 2H × 2 protons adjacent to the amide bond), 3.47−3.54 (m, 3H × 50, 4H × 264, $-CH_2-CH(CH_3)-O-$ of PPO and $-CH_2-CH_2-O-$ of PEO), 7.17 (t, J = 6 Hz, 1H × 2, amidic NH). IR (solid state, cm^{-1}) ν = 2885 (s), 1716 (w).

Synthesis of Folate-Conjugated Pluronic F108 (F108-FA). F108-NH_2 (0.498 g, 0.034 mmol), *N*-hydroxysuccinimmide (NHS, 0.033 g, 0.29 mmol), *N*,*N*′-dicyclohexylcarbodiimide (DCC, 0.055 g, 0.27 mmol), and folic acid (FA, 0.053 g, 0.12 mmol) were dissolved in 10 mL of DMSO in the presence of triethylamine (50 μL). The reaction mixture was stirred for 24 h at room temperature under a nitrogen atmosphere. Twenty milliliters of deionized water was added to the reaction mixture to precipitate DCU (dicyclohexylurea), and then the mixture was centrifuged and the supernatant was dialyzed (molecular weight cutoff of the dialysis tube was 14 kDa) for 3 days against deionized water, which was changed every 3−6 h. The resulting product was lyophilized for 3 days in order to remove all of the residual water. Yield: 45% (0.230 g, 0.015 mmol); mp: 145 °C. ^{1}H NMR (300 MHz, DMSO-d_6, 298 K): δH 1.03 (d, J = 6 Hz; 3H × 50, $-CH_3$ of PPO), 3.47−3.54 (m, 3H × 50, 4H × 264, $-CH_2-CH(CH_3)-O-$ of PPO and $-CH_2-CH_2-O-$ of PEO), 6.63 (d, J = 9 Hz, 2H × 2 of the phenilic ring), 6.88 (t, J = 7.5 Hz, 1H × 2, aryl NH), 7.10−7.30 (m, 1H × 2, amidic NH from the precursor), 7.50−7.80 (m, 2H × 2, of the phenilic ring), 7.80−8.10 (m, 1H × 2, amidic NH), 8.66 (s, 1H × 2, pteridinic CH). IR (solid state, cm^{-1}) ν = 2885 (s), 1608, 1642, 1689, 1723 (w).

Sample Preparation. Monoolein-based cubosomes were prepared and stabilized by dispersing the appropriate amount of MO in water solutions of different F108/F108-FA mixtures (100:0, 90:10, 80:20, 60:40, 50:50, 30:70, and 0:100 wt %/wt %) using an UP100H ultrasonic processor developed by Hielscher, cycle 0.9, amplitude 90%, for 10 min. Doped cubosomes were obtained by dispersing the fluorophore and the drug in the melted monoolein with the help of an ultrasonic bath before dispersion in the stabilizer solution. The sample volume was usually 4 mL with approximately 96.4 wt % water, 3.3 wt % MO, and 0.3 wt % Pluronics mixture. Fluorophore and camptothecin quantities were, respectively, 2.8 × 10^{-4} and 4.0 × 10^{-4} wt %.

Dialysis and Drug-Loading Efficiency (*E*%). After drug loading, cubosome dispersions were purified from the nonencapsulated drug by dialysis as follows: 2 mL was loaded into a dialysis tubing cellulose membrane (14 kDa MW cutoff, purchased from Sigma-Aldrich) and dialyzed against water (1000 mL) for 2 h (by replacing the water after 1 h) at 5 °C. The drug-loading efficiency, expressed as a percentage of the initially used amount of drug, was determined by UV−vis spectroscopy after the disruption of cubosomes with acetonitrile. Camptothecin and fluorophore contents were quantified respectively at 363 and 755 nm using a Thermo Nicolet Evolution 300 UV−vis spectrophotometer.

Cryogenic Transmission Electron Microscopy (Cryo-TEM). Vitrified specimens were prepared in a controlled-environment vitrification system (CEVS) at 25 °C and 100% relative humidity. A drop of the sample was placed on a perforated carbon film-coated copper grid, blotted with filter paper, and plunged into liquid ethane at its freezing point. The vitrified specimens were transferred to a 626 Gatan cryo-holder and observed at a 120 kV acceleration voltage in an FEI Tecnai T12 G^2 transmission electron microscope at about −175

dx.doi.org/10.1021/la501332u | *Langmuir* 2014, 30, 6228−6236

Scheme 1. Reaction Scheme Adopted for the Synthesis of F108-FA

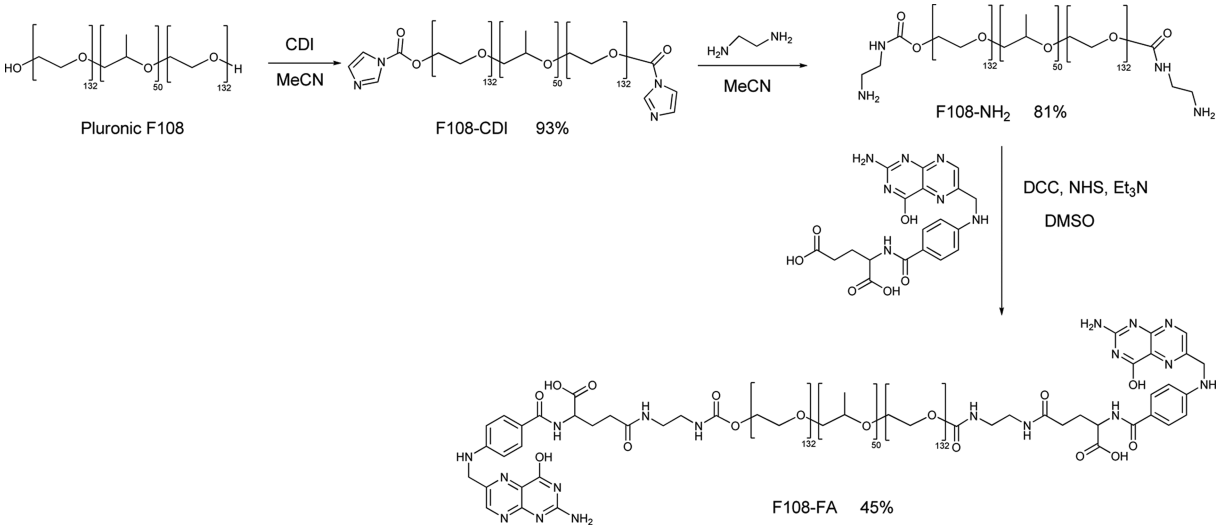

°C in low-dose imaging mode to minimize electron-beam radiation damage. Images were digitally recorded with a Gatan US1000 high-resolution CCD camera.

Dynamic Light Scattering (DLS). Particle size and ζ-potential determinations of the nanoparticles were performed with a ZetaSizer Nano ZS (Malvern Instruments, Malvern, U.K.) at a temperature of 25 ± 0.1 °C. Samples were backscattered by a 4 mW He−Ne laser (operating at a wavelength of 633 nm) at an angle of 173°. Diluted samples (1:50) were housed in disposable polystyrene cuvettes of 1 cm optical path length with water as the solvent. At least two independent samples were taken, each of which was measured three to five times. The autocorrelation function (ACF) of scattered light intensity was converted to the ACF of the scattered electric field. From this last quantity, the software supplied by the producer evaluates the *z*-averaged hydrodynamic diameter (D_{av}) and the variance of the intensity-weighted size distribution function through cumulant analysis (second order) and subsequent application of the Stokes−Einstein equation. The intensity-weighted size distribution function, i.e., the fraction of the light intensity scattered by particles of different size, was also recovered by taking the inverse Laplace transform of the ACF using the software implemented by the manufacturer. In all cases, the intensity-weighted size distribution functions were monomodal with mean and variance indistinguishable from those recovered through cumulant analysis. The hydrodynamic diameter distribution is indicated by the PDI (polydispersion index).

Small-Angle X-ray Scattering (SAXS) Experiments. Small-angle X-ray scattering was recorded with a S3-MICRO SWAXS camera system (HECUS X-ray Systems, Graz, Austria). Cu Kα radiation of wavelength 1.542 Å was provided by a GeniX X-ray generator, operating at 50 kV and 1 mA. A 1D-PSD-50 M system (HECUS X-ray Systems, Graz, Austria) containing 1024 channels of width 54.0 μm was used for the detection of scattered X-rays in the small-angle region. The working q range (Å^{-1}) was $0.003 \leq q \leq 0.6$, where $q = 4\pi \sin(\theta)\lambda^{-1}$ is the scattering wave vector. For the analysis, thin-walled 2 mm glass capillaries were filled with the cubosome dispersions. The diffraction patterns of cubosomes were recorded for 2 h. The lattice parameter a of the cubic phases was determined using the relation $a = d(h^2 + k^2 + l^2)^{1/2}$ from linear fits of the plots of $1/d$ versus $(h^2 + k^2 + l^2)^{1/2}$, where $d = 2\pi/q$ (q is the measured peak position) and h, k, and l are the Miller indices. Water channel radii were calculated using the relation $R_w = [(A_0/-2\pi\chi)^{1/2}a] - L$, where L is the lipid length value (17 Å), a is the lattice parameter obtained from the SAXS analysis, and A_0 and χ are the surface area and the Euler characteristic of the IPMS geometries ($Pn3m$, $A_0 = 1.919$, $\chi = -2$). To minimize scattering from air, the camera volume was kept under vacuum during the measurements. Silver behenate ($CH_3-(CH_2)_{20}-COOAg$) with a d spacing value of 58.38 Å was used as a standard to calibrate the angular scale of the measured intensity.

Photophysical Measurements. Cubosome solutions were diluted with Milli-Q water. UV−vis absorption spectra were recorded at 25 °C with a PerkinElmer Lambda 45 spectrophotometer. Quartz cuvettes with an optical path length of 1 cm were used. Corrected fluorescence emission and excitation spectra (450 W Xe lamp) were obtained with an Edinburgh Instruments FLS920 modular UV−vis−NIR spectrofluorimeter equipped with a Hamamatsu R928P P photomultiplier tube (for the 500−850 nm spectral range) and an Edinburgh Instruments Ge detector (for the 800−1600 nm spectral range). The same instrument connected to a PCS900 PC card was used for the TCSPC (time-correlated single-photon counting) experiments (excitation laser λ = 405 nm). Corrections for instrumental response, inner filter effects, and phototube sensitivity were performed.[45] All fluorescence anisotropy measurements were performed on an Edinburgh FLS920 equipped with Glan-Thompson polarizers. Anisotropy measurements were carried out by an L-format configuration, and all data were corrected for polarization bias using the G factor.

Cell Culture and Treatments. Human carcinoma cell line HeLa (ATCC collection) was grown in phenol red-free Dulbecco's modified Eagle's medium (DMEM, Invitrogen, USA) with high glucose, supplemented with 10% (v/v) fetal bovine serum, penicillin (100 U mL^{-1}), and streptomycin (100 μg mL^{-1}) (Invitrogen) in a 5% CO_2 incubator at 37 °C. Cells were seeded in 35 mm dishes, and experiments were carried out 2 days after seeding, when cells had reached 90% confluency. Cubosomes (1:500, 4 μL in 2 mL of free-serum medium) were added to the cells and incubated at 37 °C for 2, 4, and 24 h. For live cell imaging, after replacing the particle suspension with fresh serum-free medium, cells were loaded with fluorescent probes, and after the incubation time, the probes were washed out before the imaging session. Cells were supravitally stained with the following probes: 300 nM Nile red (NR) (9-diethylamino-5H-benzo[a]phenoxazine-5-one) for 15 min and 650 nM Hoechst 33258 (HOE) for 30 min. Vehicles were DMSO for NR and water for HOE. Stock solutions were 1000-fold concentrated not to exceed the 0.1% concentration of vesicles in the medium. Nile red was from Fluka (Buchs, SG, Switzerland); Hoechst was from Sigma-Aldrich (St. Louis, MO, USA).

Fluorescence Microscopy. Light microscopy observations were made with a Zeiss (Axioskop) upright fluorescence microscope (Zeiss, Oberkochen, Germany) equipped with 10×, 20×, and 40×/0.75 NA water-immersion objectives and an HBO 50 W L-2 mercury lamp (Osram, Berlin, Germany). Twelve-bit-deep images were acquired with a monochrome-cooled CCD camera (QICAM, Qimaging, Canada) with variable exposure. For the observation of the HOE

dx.doi.org/10.1021/la501332u | *Langmuir* 2014, 30, 6228−6236

Table 1. Space Group, Lattice Parameter (a), Water Channel Radius (r_W), Mean Diameter (D_{av}), Polydispersion Index (PDI), ζ Potential, and Stability of the Cubosome Nanoparticles Stabilized with Different F108/F108-FA Ratios (Wt %)[a]

F108/F108-FA	space group	a (Å)	r_W (Å)	D_{av} (nm)	PDI	ζ potential (mV)	stability (weeks)
100/0	*Pn*3*m*	99 ± 2	22 ± 1	133 ± 1	0.11	−28 ± 2	>24
90/10	*Pn*3*m*	95 ± 1	20 ± 1	135 ± 3	0.13	−20 ± 1	>24
80/20	*Pn*3*m*	97 ± 2	21 ± 1	139 ± 3	0.11	−29 ± 1	>24
60/40	*Pn*3*m*	100 ± 1	22 ± 1	142 ± 1	0.13	−29 ± 1	18
50/50	*Pn*3*m*	93 ± 1	19 ± 1	151 ± 1	0.13	−23 ± 1	18
30/70	*Pn*3*m*	99 ± 1	22 ± 1	159 ± 2	0.12	−25 ± 1	2
0/100	*Pn*3*m*	96 ± 1	20 ± 1	168 ± 1	0.13	−25 ± 1	2
80/20 + drug	*Pn*3*m*	102 ± 1	23 ± 1	145 ± 2	0.14	−23 ± 1	>24
80/20 + drug + dye	*Pn*3*m*	102 ± 1	23 ± 1	141 ± 1	0.12	−25 ± 1	>24

[a]Errors are reported as mean ± SD.

probe, the filters were ex 360 ± 20 nm and em 460 ± 25 nm. For NR, the filters were ex 470 ± 20 nm and em 535 ± 40 nm for nonpolar lipids and ex 546 ± 6 nm and em 620 ± 60 nm for total lipids. The adopted filters allowed a virtually complete separation of the emissions and the simultaneous observation of NR and HOE probes. Image alignments were obtained with Image Pro Plus software.

Lipid Droplet Staining and Quantification. Cells were seeded in 35 mm dishes and cultured in serum-containing media. After nanoparticle treatments, cells were stained with NR and HOE. NR is an ideal probe for the detection of lipids, as it exhibits high affinity, specificity, and sensitivity to the degree of hydrophobicity of lipids. The latter feature results in a shift of the emission spectrum from red to green in the presence of polar and nonpolar lipids, respectively.[46] For this reason, in staining living cells with NR, cytoplasmic membranes are stained red, whereas neutral lipids of lipid droplets are stained green. Fluorescent images of NR-stained cells were acquired at 10× and 40× magnifications of a fluorescence microscope. Measurements, made on a single-cell basis, gave the amount of lipid droplet content, evaluated by the fluorescence intensity of NR-green emission. The IOD (integrated optical density) per cell was calculated using Image ProPlus software (Media Cybernetics, Silver Springs, MD).

Confocal Microscopy. Measurements were performed on mounted slides by a Leica TCS SP5 SM (Leica Microsystems, Mannheim, Germany) inverted confocal microscope. For Hoechst (nuclear stain), excitation was provided by a 405 nm 40 MHz pulsed laser diode (Picoquant, Berlin, Germany), whereas the 458 nm laser line of a cw Ar laser was used to excite the dye. In both cases, the typical excitation average power was in the 100−800 μW range, when measured after the objective. Hoechst emission was collected at 420−480 nm by the internal monochromator of the microscope interfaced with a photomultiplier detector. Dye emission was filtered at wavelengths >680 nm by an interferential filter (Semrock, Rochester, NY, USA) and collected by one avalanche photodiode detector (Picoquant, Berlin, Germany). The confocal pinhole was set to a 1 Airy size; a 100× 1.4 NA objective was used for all measurements. The line-scanning speed was 400−700 Hz in standard acquisition mode.

RESULTS AND DICUSSION

Cubosomes Characterization. Here, the use of monoolein (MO)-based cubosomes as nanoparticles for the active targeting of cancer cells was investigated. For this purpose, the surfactant used to stabilize cubosomes (Pluronic F108, F108) was conjugated to folate[47] (Scheme 1), a targeting ligand which displays a high affinity for the folate receptor overexpressed on the tumor cell membrane. Briefly, F108, initially activated with CDI, was reacted with ethylenediamine to obtain amine-terminated F108, and the resulting F108-NH_2 was finally reacted with NHS, DCC, Et_3N, and folic acid (see Supporting Information for characterization details). The purity of F108-FA and then the absence of unreacted F108-NH_2 were confirmed by a thin-layer ninhydrin assay. Furthermore, after the pH value was decreasing to 2, there was no precipitation of unreacted folic acid.[48]

Subsequently, mixtures of F108 and its folate-conjugated counterpart were used to stabilize the aqueous cubosome dispersions. At first, the physicochemical characterization of cubosome nanoparticles stabilized with different F108/F108-FA ratios was performed by SAXS and DLS. The results are summarized in Table 1. As can be seen from the SAXS data, nanoparticles retained the *Pn*3*m* structure found in traditional cubosomes (i.e., those prepared with 100% F108), with no significant variations in the lattice parameter, even after the complete substitution of F108 with F108-FA. Conversely, the DLS analysis indicated that the amount of F108-FA used to stabilize nanoparticles strongly affected the mean particles size, which increased from 133 nm (100% F108) to 168 nm (100% F108-FA). Although a slight increase in the PDI was detected upon decreasing the F108/F108-FA ratio, independently by the presence of the folate-conjugated Pluronic, the various solutions consisted mainly of homogeneous cubosome dispersions. The nanoparticles growth was also confirmed by SAXS experiments because while increasing the amount of F108-FA the profile of the quasi-Bragg peaks became sharper (Figure 1). Indeed, the absence of well-defined Bragg peaks in

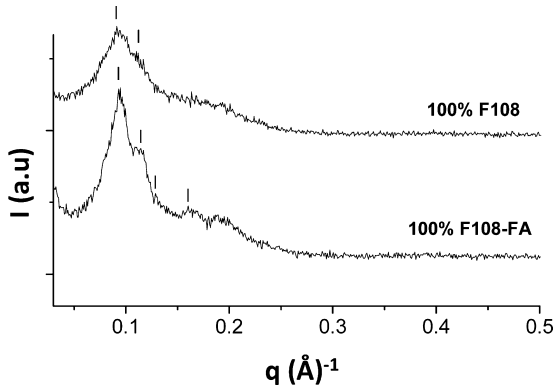

Figure 1. SAXS patterns of cubosome dispersions stabilized by F108 and F108-FA Pluronics. Relevant peaks are indicated.

SAXS patterns of cubosome dispersions is typically related to the very small nanoparticle size (in which the peak width is inversely proportional to the crystalline domain size). Therefore, the quasi-Bragg peaks' appearance in the sample containing 100% F108-FA represents an additional proof of the increased size of the nanoparticles.

dx.doi.org/10.1021/la501332u | *Langmuir* 2014, 30, 6228−6236

Concerning the measured ζ-potential values (reported in Table 1), they were found to be in the range of −20 to −30 mV, almost equivalent to those of nontargeted cubosomes (−28 mV), with some fluctuations that appeared independently of the F108/F108-FA ratio. Nevertheless, the stability over time was found to depend greatly on the F108-FA content because samples prepared with a higher percentage of F108-FA exhibited a reduced shelf life, as demonstrated by the observed phase separation (Table 1).

The role of Pluronics in this kind of formulation consists of stabilizing the obtained nanoparticles against coalescence or coagulation basically via mixing and entropic effects.[2] Therefore, the reported experimental findings suggest that the conjugation of the folate to the terminal end of the PEO moieties greatly modifies the original stabilizing properties of F108, thus producing the observed alteration in cubosome formulations when F108 is gradually replaced by F108-FA. Indeed, it is likely that such a conjugation destabilizes the delicate balance between the PEO−solvent and PEO−PEO interactions, on the basis of the mixing effect, thus leading to the observed changes in size and stability of the cubosomes. In other words, the regular increase in the nanoparticles' hydrodynamic radii as well as the reduced stability and the increased PDI of the cubosome dispersions while the F108-FA content is increased is strong evidence of the less effective dispersant and stabilizing properties of F108-FA with respect to those of F108.

Given the potential biomedical application of these formulations and on the basis of the stability tests, the cubosome dispersion stabilized with mixture F108/F108-FA = 80/20 (wt %) was selected for loading with the anticancer drug camptothecin (Scheme 2), which, along with its analogues, has been demonstrated to be effective against a broad spectrum of tumors.[49−51]

Scheme 2. Chemical Sturucture of Camptothecin (Left) and NIR Dye 2,4-Di-3-guaiazulenyl-1,3-dihydroxycyclobutenediylium Dihydroxide Bis(inner salt) (Right)

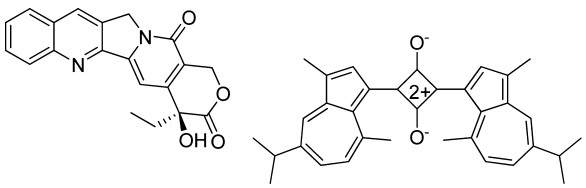

SAXS and DLS revealed that inclusion of camptothecin (a highly hydrophobic drug) within the lipid bilayer basically did not alter the cubosome nanostructure. The morphology of these nanoparticles was observed by cryo-TEM (Figure 2). Several nanoparticles with inner cubic structure are clearly discernible, along with the vesicular structures often seen in cubosome formulations. By means of repeated observations, the sample that was investigated was found to be a dispersion of cubosomes having a diameter of 100−200 nm, in good agreement with the dimensions obtained by DLS. It is worth noticing that all of the size distributions obtained from DLS appeared to be monomodal with mean sizes ranging from 133 to 168 nm. At variance, an inspection of TEM images reveals the coexistence of large cubosomes with small unilamellar vesicles. This is because the ACF (Experimental Section) measured in DLS reflects the intensity-weighted size distribution function, i.e., the fraction of the light intensity scattered by particles of different sizes. Since the efficiency of light scattering increases dramatically with particle size, such a size distribution is heavily biased toward large particles, and the presence of large cubosomes fully dominates the correlogram. Cryo-TEM experiments performed on targeted cubosomes not containing the drug (data not shown) revealed that they possess an identical nanostructure with respect to those loaded with camptothecin and the dye. The loading efficiencies (E%) for the drug and the fluorophore were found to be 71 and 95%, respectively.

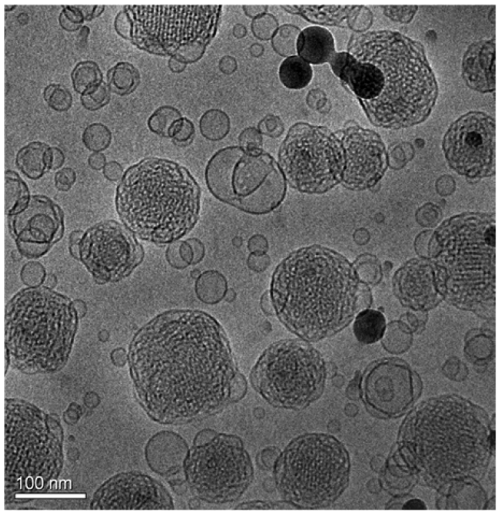

Figure 2. Cryo-TEM image of MO-based cubosomes containing both the drug and the dye and stabilized by the mixture F108/F108-FA = 80/20.

NIR Fluorescent Probe Characterization. The absorption spectrum of an aqueous suspension of cubosomes loaded with both camptothecin and NIR dye 2,4-di-3-guaiazulenyl-1,3-dihydroxycyclobutenediylium dihydroxide bis(inner salt) (Scheme 2) did not show any characteristic band because the turbidity of the suspension originated strong light scattering. However, a shoulder at around 760 nm ascribable to the dye could be observed (data no shown). When excited at 340 nm, an unstructured emission band at 428 nm (Figure 3a) with an excited-state lifetime of 0.6 ns, which can be assigned to camptothecin,[52−54] was observed. Moreover, an emission band with a maximum at 938 nm was observed when exciting the sample at 418 nm (Figure 3b). The fluorescence anisotropy measurement at 938 nm (r = 0.1) suggested that the dye has reduced mobility, indicating that it is enclosed in the nanoparticle. This conclusion is also supported by the insolubility of the dye in pure water. (The absorption and emission spectra of an aqueous solution of the dye did not show any of the characteristic bands of the fluorophore.)

Lipid Droplet Evaluation. The selective cellular uptake of targeted cubosomes was investigated via IOD analysis by observing the lipid droplet (LD) formation in HeLa cells after treatment with the monoolein-based nanoparticles following a previously developed protocol.[12] LDs are cytoplasmic organelles consisting of a hydrophobic core of neutral lipids (such as triglycerides and cholesterol esters) encased by a phospholipid monolayer harboring a set of enzymes and regulatory proteins, which catalyze the metabolically controlled synthesis and mobilization of fat stores.[55] LD formation is a regulated cellular process that culminates in the compartmentalization of

dx.doi.org/10.1021/la501332u | Langmuir 2014, 30, 6228−6236

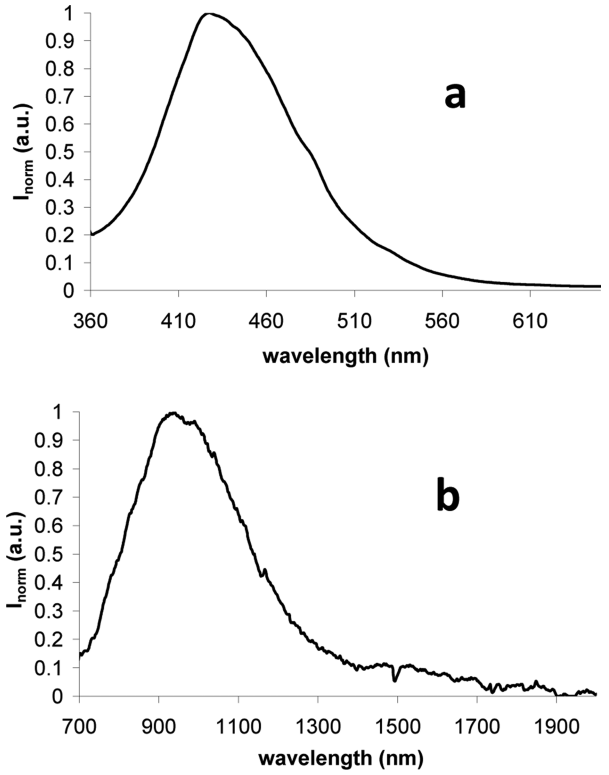

Figure 3. Normalized emission of an aqueous dispersion of targeted cubosomes (stabilized with the mixture F108/F108-FA = 80/20) loaded with camptothecin and the NIR-emitting dye. (a) Emission band of camptothecin at 428 nm (λ_{exc} = 340 nm); (b) emission band of the dye at 938 nm (λ_{exc} = 418 nm).

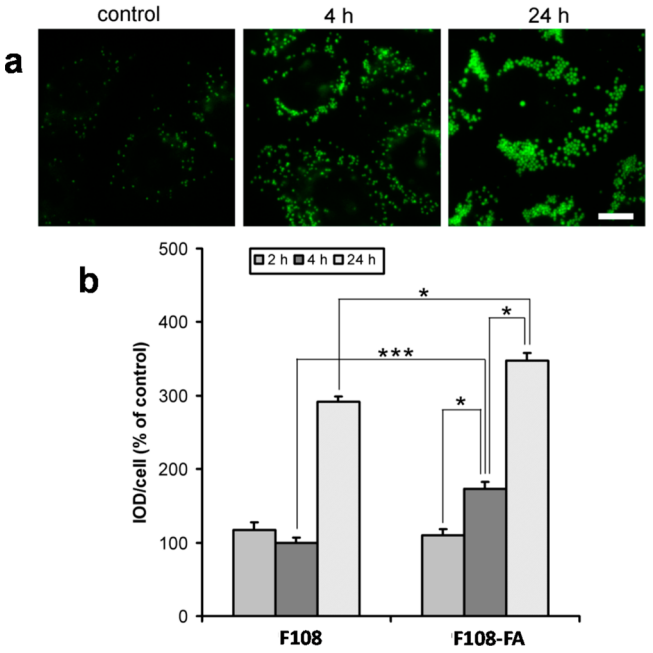

Figure 4. Lipid droplet accumulation induced in HeLa cells by cubosome treatment. (a) Representative color images of nontreated HeLa cells (control) and cells exposed to the monoolein-based cubosomes dispersed through a 80/20 mixture of F108/F108-FA at 4 and 24 h of incubation time. Scale bar = 20 μm. (b) Results of lipid droplet formation at different incubation times. Data are expressed as the mean ± SD from at least two independent experiments. Statistically significant differences are indicated by * ($p < 0.05$) and *** ($p < 0.0001$) via the t test.

lipids, when long-chain unsaturated fatty acids, such as oleic acid, are available from exogenous sources inside the cells.[56] Indeed, after entering the cells, unsaturated fatty acids are rapidly activated, esterified, and stored as triglycerides inside the lipid droplets. Therefore, detecting changes in LD formation and size may be useful in differentiating between targeted and traditional cubosome uptake.

Within this scope, HeLa cells, used as model cancer cells since they express high levels of folate receptors,[57] were exposed at different times to both types of cubosomes coloaded with NR and HOE probes to identify LDs and nuclear morphology, respectively. The IOD per cell value of nontreated control cells was set to 100%, and values of cubosome-treated cells were expressed as a percentage of control. Results are reported in Figure 4a,b.

At a short incubation time (2 h) with targeted cubosomes, the size and number of LDs, detectable as punctuated green fluorescent cytoplasmic structures dispersed throughout the cytoplasm, did not show significant differences in comparison to treated nontargeted cubosomes and untreated control cells. On the contrary, statistically significant differences were observed after 4 h of incubation. In those cells, a noteworthy increase in the IOD per cell of 1.6-fold ($p < 0.05$) was estimated with targeted cubosomes, in comparison to the 2 h treatment and 1.8-fold ($p < 0.001$) increase in comparison to that of nontargeted cubosomes. In contrast, the latter did not show significant differences in comparison to the 2 h treatment. At a longer exposure time (24 h), both nanoparticles were effectively internalized. However, treatment with targeted cubosomes caused a 1.2-fold increase ($p < 0.05$) in the IOD/cell in comparison to that of nontargeted nanoparticles (2.9- and 3.5-fold increases ($p < 0.0001$) in traditional and FA-containing cubosomes, respectively, versus the control). At this time, LDs appeared as fluorescent bright spots with a globular shape that were more numerous and larger in a remarkable way (1 to 2 μm diameter). Importantly, neither a sign of morphological damage nor chromatin condensation (Hoechst positive nuclei) was observed after both types of nanoparticle treatment (data not shown).

Confocal Microscopy. HeLa cells treated with dye-unloaded (control) or dye-loaded cubosomes were imaged by confocal microscopy after fixation with 4% paraformaldehyde for 10 min at room temperature (Figure 5). Note that chromatin was also stained with the Hoechst marker to identify the positions of cell nuclei (Figure 5b,e). Since the dye is infrared-emitting, fluorescence collection at >680 nm was obtained by using a single-photon avalanche photodiode with 30 and 5% photon sensitivities at 700 and 900 nm, respectively.

An inspection of control cells reveals that some autofluorescence is produced in the IR region of fluorescence collection upon excitation at 458 nm (Figure 5c). However, dye-loaded cells display significant differences in the morphology and distribution of emitters (Figure 5f). In fact, the dye-treated cells display a bright, cell-wide emission background together with large emitting perinuclear spots, while both features are nearly absent in control cells. (Note that panels c and f share the same fluorescence pseudocolor scale, i.e., the intensity differences are real.) Overall, these findings are consistent with an internalization of the dye mediated by cubosome nanocarriers.

dx.doi.org/10.1021/la501332u | Langmuir 2014, 30, 6228−6236

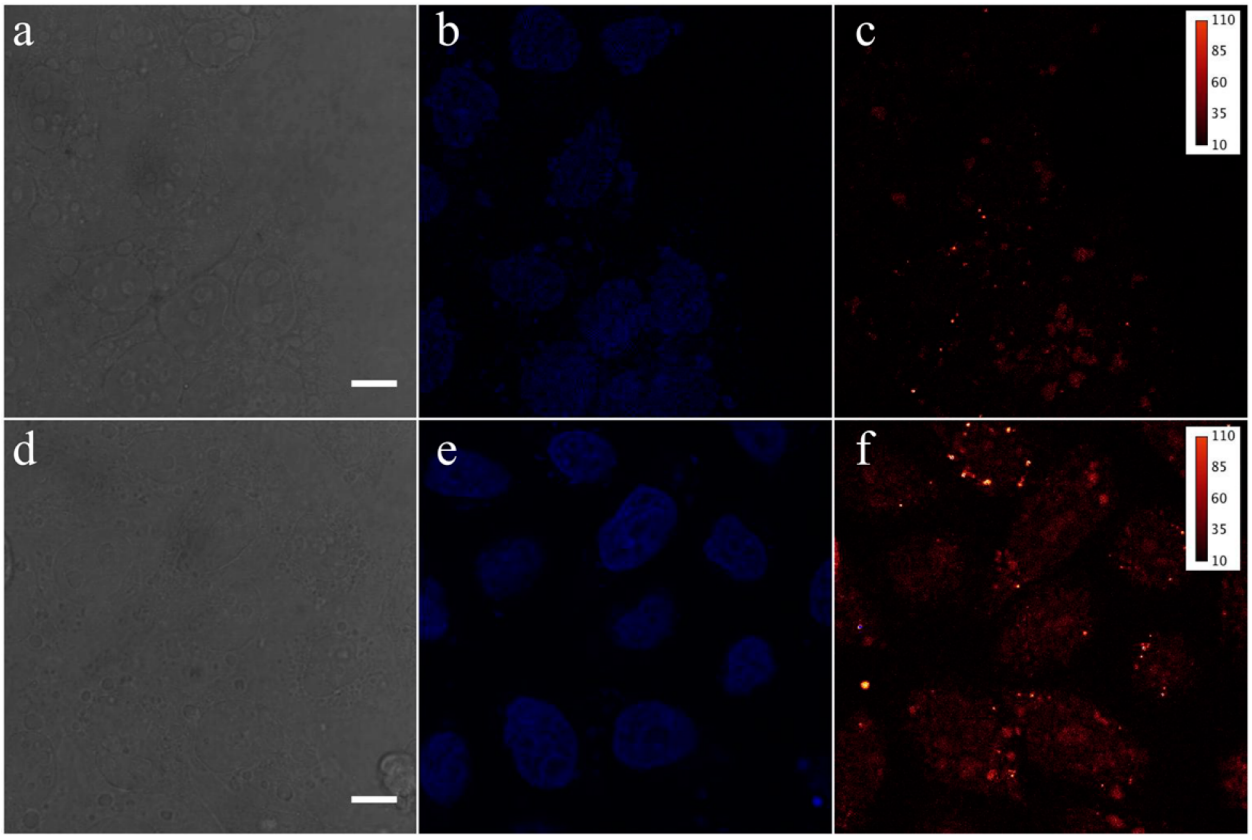

Figure 5. Fluorescence microscopy images of HeLa cells treated with dye-free (a–c) or dye-loaded cubosomes (d–f). (a, d) Transmission micrographs of cells; scale bar = 10 μm. (b, e) Fluorescence micrographs collected in the 420–480 nm interval where nuclear marker Hoechst emits. (c, f) Fluorescence micrographs collected at >680 nm where the dye emits; both images display fluorescence according to the same pseudocolor intensity scale (inset).

CONCLUSIONS

Recent works suggested the possibility of using cubosomes in theranostic nanomedicine.[40,58,59] Here, the potential use of cubosomes as theranostic nanoparticles also having targeting properties was explored. The physicochemical investigations proved that these nanoparticles, still retaining their inner nanostructure, can be effectively stabilized by mixtures of Pluronic F108 and folate-conjugated F108. Furthermore, it was demonstrated that camptothecin, a potent anticancer drug, and an NIR-emitting fluorescent probe (a squaraine) can be successfully loaded within the cubosomes. Finally, the cellular uptake of these innovative nanocarriers was monitored on HeLa cells. Following the indication given by the cell lipid droplets in terms of their increase in number and growth in size, the superior performance of the cubosomes stabilized through the F108 and folate-conjugated F108 Pluronics mixtures was confirmed. Indeed, even if at longer treatment times (24 h) both targeted and nontargeted cubosomes were effectively internalized and differences were partially leveled out, results collected at short incubation time (4 h) clearly evidenced that the conjugation of Pluronic with folate speeds the cubosomes uptake as a result of receptor–ligand interactions.

On the whole, the results presented here validate cubosomes as a useful platform for theranostic nanomedicine.

ASSOCIATED CONTENT

Supporting Information

Detailed description of the folate-conjugated Pluronic F108 synthesis. This material is available free of charge via the Internet at http://pubs.acs.org.

AUTHOR INFORMATION

Corresponding Authors

*Tel: +390706754453. E-mail: ccaltagirone@unica.it.
*Tel: +390706754453. E-mail: murgias@unica.it

Notes

The authors declare no competing financial interest.

ACKNOWLEDGMENTS

We thank Gerardo Palazzo for fruitful discussions and acknowledge Giulia Battistelli for her help with the photophysical experiments. Financial support by MIUR (projects PRIN2009-2009Z9ASCA and PRIN 2010BJ23MN_002) and Regione Autonoma della Sardegna (CRP-59699) is gratefully acknowledged. Sardegna Ricerche Scientific Park (Pula, CA, Italy) is acknowledged for free access to the facilities of the Nanobiotechnology Laboratory. The cryo-TEM work was performed at the Technion Laboratory for Electron Microscopy of Soft Matter, supported by the Technion Russell Berrie Nanotechnology Institute (RBNI).

REFERENCES

(1) Angelico, R.; Ceglie, A.; Colafemmina, G.; Lopez, F.; Murgia, S.; Olsson, U.; Palazzo, G. Biocompatible lecithin organogels: Structure and phase equilibria. *Langmuir* **2005**, *21*, 140−148.

(2) Chong, J. Y. T.; Mulet, X.; Waddington, L. J.; Boyd, B. J.; Drummond, C. J. Steric stabilisation of self-assembled cubic lyotropic liquid crystalline nanoparticles: high throughput evaluation of triblock polyethylene oxide-polypropylene oxide-polyethylene oxide copolymers. *Soft Matter* **2011**, *7*, 4768−4777.

(3) Hiwale, P.; Lampis, S.; Conti, G.; Caddeo, C.; Murgia, S.; Fadda, A. M.; Monduzzi, M. In vitro release of lysozyme from gelatin microspheres: effect of cross-linking agents and thermoreversible gel as suspending medium. *Biomacromolecules* **2011**, *12*, 3186−3193.

(4) Kumari, A.; Yadav, S. K.; Yadav, S. C. Biodegradable polymeric nanoparticles based drug delivery systems. *Coll. Surf. B: Biointerfaces* **2010**, *75*, 1−18.

(5) Murgia, S.; Fadda, P.; Colafemmina, G.; Angelico, R.; Corrado, L.; Lazzari, P.; Monduzzi, M.; Palazzo, G. Characterization of the Solutol® HS15/water phase diagram and the impact of the Δ9-tetrahydrocannabinol solubilization. *J. Colloid Interface Sci.* **2013**, *390*, 129−136.

(6) Bonacchi, S.; Genovese, D.; Juris, R.; Montalti, M.; Prodi, L.; Rampazzo, E.; Zaccheroni, N. Luminescent Silica Nanoparticles: Extending the Frontiers of Brightness. *Angew. Chem., Int. Ed.* **2011**, *50*, 4056−4066.

(7) Rampazzo, E.; Voltan, R.; Petrizza, L.; Zaccheroni, N.; Prodi, L.; Casciano, F.; Zauli, G.; Secchiero, P. Proper design of silica nanoparticles combine high brightness, lack of cytotoxicity and efficient cell endocytosis. *Nanoscale* **2013**, *5*, 7897−7905.

(8) Lee, N.; Hyeon, T. Designed synthesis of uniformly sized iron oxide nanoparticles for efficient magnetic resonance imaging contrast agents. *Chem. Soc. Rev.* **2012**, *41*, 2575−2589.

(9) Ling, D.; Hyeon, T. Iron oxide nanoparticles: chemical design of biocompatible iron oxide nanoparticles for medical applications. *Small* **2013**, *9*, 1449−1449.

(10) Zhang, Y.; Sun, Y.; Xu, X.; Zhang, X.; Zhu, H.; Huang, L.; Qi, Y.; Shen, Y.-M. Synthesis, biodistribution, and microsingle photon emission computed tomography (SPECT) imaging study of technetium-99m labeled PEGylated dendrimer poly (amidoamine)-(PAMAM) - folic acid conjugates. *J. Med. Chem.* **2010**, *53*, 3262−3272.

(11) Angelico, R.; Carboni, M.; Lampis, S.; Schmidt, J.; Talmon, Y.; Monduzzi, M.; Murgia, S. Physicochemical and rheological properties of a novel monoolein-based vesicle gel. *Soft Matter* **2013**, *9*, 921−928.

(12) Carboni, M.; Falchi, A. M.; Lampis, S.; Sinico, C.; Manca, M. L.; Schmidt, J.; Talmon, Y.; Murgia, S.; Monduzzi, M. Physicochemical, cytotoxic, and dermal release features of a novel cationic liposome nanocarrier. *Adv. Healthcare Mater.* **2013**, *2*, 692−701.

(13) Cuomo, F.; Mosca, M.; Murgia, S.; Avino, P.; Ceglie, A.; Lopez, F. Evidence for the role of hydrophobic forces on the interactions of nucleotide-monophosphates with cationic liposomes. *J. Colloid Interface Sci.* **2013**, *410*, 146−151.

(14) Gillies, E. R.; Frechet, J. M. J. Dendrimers and dendritic polymers in drug delivery. *Drug Discuss. Today* **2005**, *10*, 35−43.

(15) Svenson, S.; Tomalia, D. A. Dendrimers in biomedical applications-reflections on the field. *Adv. Drug Delivery Rev.* **2012**, *64*, 102−115.

(16) Klostranec, J. M.; Chan, W. C. W. Quantum dots in biological and biomedical research: recent progress and present challenges. *Adv. Mater.* **2006**, *18*, 1953−1964.

(17) Nam, J.; Won, N.; Bang, J.; Jin, H.; Park, J.; Jung, S.; Jung, S.; Park, Y.; Kim, S. Surface engineering of inorganic nanoparticles for imaging and therapy. *Adv. Drug Delivery Rev.* **2013**, *65*, 622−648.

(18) Zrazhevskiy, P.; Sena, M.; Gao, X. Designing multifunctional quantum dots for bioimaging, detection, and drug delivery. *Chem. Soc. Rev.* **2010**, *39*, 4326−4354.

(19) Choi, K. Y.; Jeon, E. J.; Yoon, H. Y.; Lee, B. S.; Na, J. H.; Min, K. H.; Kim, S. Y.; Myung, S.-J.; Lee, S.; Chen, X. Theranostic nanoparticles based on PEGylated hyaluronic acid for the diagnosis, therapy and monitoring of colon cancer. *Biomaterials* **2012**, *33*, 6186−6193.

(20) Choi, K. Y.; Liu, G.; Lee, S.; Chen, X. Theranostic nanoplatforms for simultaneous cancer imaging and therapy: current approaches and future perspectives. *Nanoscale* **2012**, *4*, 330−342.

(21) Cohen, Y.; Shoushan, S. Y. Magnetic nanoparticles-based diagnostics and theranostics. *Curr. Opin. Biotechnol.* **2013**, *24*, 672−681.

(22) Kim, C. S.; Tonga, G. Y.; Solfiell, D.; Rotello, V. M. Inorganic nanosystems for therapeutic delivery: status and prospects. *Adv. Drug Delivery Rev.* **2013**, *65*, 93−99.

(23) Li, S.; Goins, B.; Zhang, L.; Bao, A. Novel multifunctional theranostic liposome drug delivery system: construction, characterization, and multimodality MR, near-infrared fluorescent, and nuclear imaging. *Bioconjugate Chem.* **2012**, *23*, 1322−1332.

(24) Rizzo, L. Y.; Theek, B.; Storm, G.; Kiessling, F.; Lammers, T. Recent progress in nanomedicine: therapeutic, diagnostic and theranostic applications. *Curr. Opin. Biotechnol.* **2013**, *24*, 1159−1166.

(25) Ryu, J. H.; Koo, H.; Sun, I.-C.; Yuk, S. H.; Choi, K.; Kim, K.; Kwon, I. C. Tumor-targeting multi-functional nanoparticles for theragnosis: new paradigm for cancer therapy. *Adv. Drug Delivery Rev.* **2012**, *64*, 1447−1458.

(26) Shin, S. J.; Beech, J. R.; Kelly, K. A. Targeted nanoparticles in imaging: paving the way for personalized medicine in the battle against cancer. *Integr. Biol.* **2013**, *5*, 29−42.

(27) Svenson, S. Theranostics: Are We There Yet? *Mol. pharmaceutics* **2013**, *10*, 848−856.

(28) Vivero-Escoto, J. L.; Huxford-Phillips, R. C.; Lin, W. Silica-based nanoprobes for biomedical imaging and theranostic applications. *Chem. Soc. Rev.* **2012**, *41*, 2673−2685.

(29) Wang, H.; Wu, Y.; Zhao, R.; Nie, G. Engineering the assemblies of biomaterial nanocarriers for delivery of multiple theranostic agents with enhanced antitumor efficacy. *Adv. Mater.* **2013**, *25*, 1616−1622.

(30) Barreto, J. A.; O'Malley, W.; Kubeil, M.; Graham, B.; Stephan, H.; Spiccia, L. Nanomaterials: applications in cancer imaging and therapy. *Adv. Mater.* **2011**, *23*, H18−H40.

(31) Brannon-Peppas, L.; Blanchette, J. O. Nanoparticle and targeted systems for cancer therapy. *Adv. Drug Delivery Rev.* **2012**, *64*, 206−212.

(32) Lu, Y.; Low, P. S. Folate-mediated delivery of macromolecular anticancer therapeutic agents. *Adv. Drug Delivery Rev.* **2012**, *64*, 342−352.

(33) Rudin, M.; Weissleder, R. Molecular imaging in drug discovery and development. *Nat. Rev. Drug. Discovery* **2003**, *2*, 123−131.

(34) Botta, M. Second coordination sphere water molecules and relaxivity of gadolinium (III) complexes: implications for MRI contrast agents. *Eur. J. Inorg. Chem.* **2000**, *2000*, 399−407 and references therein..

(35) Shields, A. F.; Grierson, J. R.; Dohmen, B. M.; Machulla, H. J.; Stayanoff, J. C.; Lawhorn-Crews, J. M.; Obradovich, J. E.; Muzik, O.; Mangner, T. J. Imaging proliferation in vivo with [F-18] FLT and positron emission tomography. *Nature medicine* **1998**, *4*, 1334−1336.

(36) Escobedo, J. O.; Rusin, O.; Lim, S.; Strongin, R. M. NIR dyes for bioimaging applications. *Curr. Opin. Chem. Biol.* **2010**, *14*, 64−70.

(37) Kiyose, K.; Kojima, H.; Nagano, T. Functional near-infrared fluorescent probes. *Chem.—Asian J.* **2008**, *3*, 506−515.

(38) Yuan, L.; Lin, W.; Zheng, K.; He, L.; Huang, W. Far-red to near infrared analyte-responsive fluorescent probes based on organic fluorophore platforms for fluorescence imaging. *Chem. Soc. Rev.* **2013**, *42*, 622−661.

(39) Beverina, L.; Salice, P. Squaraine compounds: tailored design and synthesis towards a variety of material science applications. *Eur. J. Org. Chem.* **2010**, *2010*, 1207−1225 and references therein..

(40) Murgia, S.; Bonacchi, S.; Falchi, A. M.; Lampis, S.; Lippolis, V.; Meli, V.; Monduzzi, M.; Prodi, L.; Schmidt, J.; Talmon, Y.; Caltagirone, C. Drug loaded fluorescent cubosomes: versatile nanoparticles for potential theranostic applications. *Langmuir* **2013**, *29*, 6673−6679.

(41) Murgia, S.; Falchi, A. M.; Mano, M.; Lampis, S.; Angius, R.; Carnerup, A. M.; Schmidt, J.; Diaz, G.; Giacca, M.; Talmon, Y.;

Monduzzi, M. Nanoparticles from lipid-based liquid crystals: emulsifier influence on morphology and cytotoxicity. *J. Phys. Chem. B* **2010**, *114*, 3518−3525.
(42) Yaghmur, A.; Glatter, O. Characterization and potential applications of nanostructured aqueous dispersions. *Adv. Colloid Interface Sci.* **2009**, *147−148*, 333−342.
(43) Fong, C.; Le, T.; Drummond, C. J. Lyotropic liquid crystal engineering-ordered nanostructured small molecule amphiphile self-assembly materials by design. *Chem. Soc. Rev.* **2012**, *41*, 1297−1322.
(44) Murgia, S.; Lampis, S.; Zucca, P.; Sanjust, E.; Monduzzi, M. Nucleotide recognition and phosphate linkage hydrolysis at a lipid cubic interface. *J. Am. Chem. Soc.* **2010**, *132*, 16176−16184.
(45) Montalti, M.; Credi, A.; Prodi, L.; Gandolfi, M. T. *Handbook of photochemistry*; 3rd ed.; CRC press, Taylor and Francis Group: Boca Raton, FL, 2006.
(46) Greenspan, P.; Mayer, E. P.; Fowler, S. D. Nile red: a selective fluorescent stain for intracellular lipid droplets. *J. Cell Biol.* **1985**, *100*, 965−973.
(47) Wei, Z.; Yuan, S.; Yanzuo, C.; Jiang, Y.; Xianyi, S.; Xiaoling, F. Multifunctional Pluronic P123/F127 mixed polymeric micelles loaded with paclitaxel for the treatment of multidrug resistant tumors. *Biomaterials* **2011**, *32*, 2894−2906.
(48) Licciardi, M.; Tang, Y.; Billingham, N. C.; Armes, S. P.; Lewis, A. L. Synthesis of novel folic acid-functionalized biocompatible block copolymers by atom transfer radical polymerization for gene delivery and encapsulation of hydrophobic drugs. *Biomacromolecules* **2005**, *6*, 1085−1096.
(49) Liu, L. F.; Desai, S. D.; Li, T.-K.; Mao, Y.; Sun, M.; Sim, S.-P. Mechanism of action of camptothecin. *Ann. N.Y. Acad. Sci.* **2000**, *922*, 1−10.
(50) Pizzolato, J. F.; Saltz, L. B. The camptothecins. *Lancet* **2003**, *361*, 2235−2242.
(51) Venditto, V. J.; Simanek, E. E. Cancer therapies utilizing the camptothecins: a review of the in vivo literature. *Mol. Pharmaceutics* **2010**, *7*, 307−349.
(52) Dey, J.; Warner, I. M. Spectroscopic and photophysical studies of the anticancer drug: camptothecin. *J. Lumin.* **1997**, *71*, 105−114.
(53) di Nunzio, M. R.; Cohen, B.; Douhal, A. Structural photodynamics of camptothecin, an anticancer drug in aqueous solutions. *J. Phys. Chem. A* **2011**, *115*, 5094−5104.
(54) Posokhov, Y.; Biner, H.; Icli, S. Spectral-luminescent and solvatochromic properties of anticancer drug camptothecin. *J. Photochem. Photobiol. A Chem.* **2003**, *158*, 13−20.
(55) Digel, M.; Ehehalt, R.; Füllekrug, J. Lipid droplets lighting up: insights from live microscopy. *FEBS letters* **2010**, *584*, 2168−2175.
(56) Fujimoto, Y.; Onoduka, J.; Homma, K. J.; Yamaguchi, S.; Mori, M.; Higashi, Y.; Makita, M.; Kinoshita, T.; Noda, J.-I.; Itabe, H. Long-chain fatty acids induce lipid droplet formation in a cultured human hepatocyte in a manner dependent of Acyl-CoA synthetase. *Biol. Pharm. Bull.* **2006**, *29*, 2174−2180.
(57) Wang, S.; Low, P. S. Folate-mediated targeting of antineoplastic drugs, imaging agents, and nucleic acids to cancer cells. *J. Controlled Release* **1998**, *53*, 39−48.
(58) Nilsson, C.; Barrios-Lopez, B.; Kallinen, A.; Laurinmäki, P.; Butcher, S. J.; Raki, M.; Weisell, J.; Bergström, K.; Larsen, S. W.; Østergaard, J.; Larsen, L.; Urtti, A.; Airaksinen, A. J.; Yaghmur, A. SPECT/CT imaging of radiolabeled cubosomes and hexosomes for potential theranostic applications. *Biomaterials* **2013**, *34*, 8491−8503.
(59) Gupta, A.; Stait-Gardner, T.; de Campo, L.; Waddington, L. J.; Kirby, N.; Price, W. S.; Moghaddam, M. J. Nanoassemblies of Gd-DTPA-monooleyl and glycerol monooleate amphiphiles as potential MRI contrast agents. *J. Mater. Chem. B* **2014**, *2*, 1225−1233.